# Ruthenium– and cobalt–based artificial metalloenzymes for photocatalytic water oxidation in artificial photosynthesis

Polanco Rivas, E.A.

# Chapter 4

## *An artificial carbonic anhydrase-ruthenium metalloenzyme for water oxidation*

This chapter will be *submitted* for publication: *An artificial carbonic anhydrase metalloprotein for water oxidation*. *Polanco E.A.; Stinger, L.; Opdam, L.V.; Bonnet, S.* and *Pandit, A. (in preparation)*

## 4.1. Introduction

Bovine Carbonic anhydrase (**BCA**) has proven to be a versatile scaffold capable of hosting diverse synthetic cofactors without decreasing their catalytic properties.[1] The mainly hydrophobic substrate-binding pocket of the protein is constituted by three histidine coordinated facially to a $Zn^{2+}$ ion. In cells, this protein is capable of catalysing the hydration of $CO_2$ gas into $H_2CO_3$, which plays an important role in the control of pH inside living cells.[2] This catalytic pocket was also demonstrated to have a great affinity with sulfonamides group, which led to the development of multiples small-molecule sulfonamide compounds that could be anchored to the **BCA** active site.[3,4] The versatility of **BCA** makes it suitable as model protein for the development of artificial metalloenzyme (ArM); it also allows for exploring the behaviour of artificial compounds in a biological aqueous environment.[5-7] Artificial photosynthesis represents one of the most appealing ways to reduce the impact of fossil fuels on our planet. Mimicking nature to use water as source of electrons is a challenging task, yet *a priori* not impossible. Still, artificial metalloenzymes capable of promoting the light-induced evolution of $O_2$ by oxidation of water, are extremely rare.[8–10] Kim and Lee reported, for example, an iridium-modified carbonic anhydrase capable of promoting dioxygen evolution with a TOF of 39.8 $min^{-1}$ at neutral pH. This work demonstrated that the protein scaffold could activate an Ir catalyst to drive this challenging reaction.[11] On the other hand, in this system it was remarked that oxygen in the photocatalytically generated $O_2$ came from the electron acceptor $NaIO_4$, rather than from water, so that the reaction was not really water oxidation.[12] Herein, we present a new artificial metalloenzymes for water oxidation anchoring a series of polypyridyl ruthenium-based water oxidation catalysts **Ru1**-**Ru4** functionalized with sulfonamide linkers (Figure 4.1).

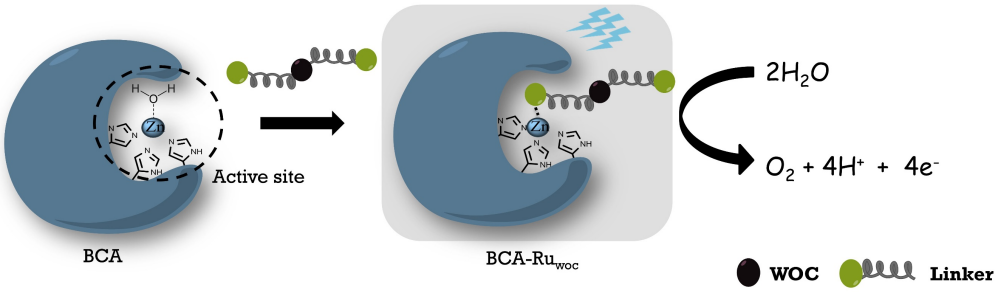


**Figure 4.1.** Schematic representation of the generation of an artificial ruthenium-functionalized bovine carbonic anhydrase. The active site is represented with three histidines of the protein backbone coordinated to $Zn^{2+}$ and one molecule of water. The active water oxidation catalyst (WOC, *black* sphere) bound to the linkers (*grey* springs) replaces the coordinated water molecule in the active site via sulfonamide ligands (*green* spheres).

## 4.2. Results

### 4.2.1 Ruthenium complexes synthesis

To anchor the known water oxidation complex [Ru(bda)(4-Mepy)$_2$] ($H_2$bda = 2,2'- bipyridine-6,6'-dicarboxylic acid)[13] to **BCA**, we developed linkers that at the same time show a high affinity for the protein binding pocket via aryl-sulfonamide groups, and can coordinate to the ruthenium center *via* pyridines. Two linkers **L1** and **L2** were synthetized characterized by different lengths between the sulfonamides and pyridine groups (Experimental section 4.5.1). For their synthesis, two benzylaminopyridines (**1** and **2**) were used as starting materials. Following modified literature procedures the functionalization of the pyridine with an aryl-sulfonamide arm was performed in one step *via* peptide coupling in presence of benzotriazol-1-yloxytris(dimethylamino)phosphonium hexafluorophosphate (BOP) as a coupling reagent and triethylamine as a base, to afford **L1** and **L2** in 78% and 62% yield, respectively.[14] To obtain the water oxidation complexes, these pyridine ligands were coordinated to [Ru(dmso)$_4$(Cl)$_2$], using $H_2$bda to afford [Ru(bda)(**L1**)$_2$] (**Ru1**) and [Ru(bda)(**L2**)$_2$] (**Ru2**),[15] and using [2,2':6',2"-terpyridine]-6,6"-dicarboxylic acid (*$H_2$tpyda*) to afford [Ru(tpyda)(**L1**)$_2$] (**Ru3**) and [Ru(tpyda)(**L2**)$_2$]

(**Ru4**).[16] Each complex was purified using size-exclusion chromatography and obtained in reasonable yields (24 to 43%, Figure 4.2).

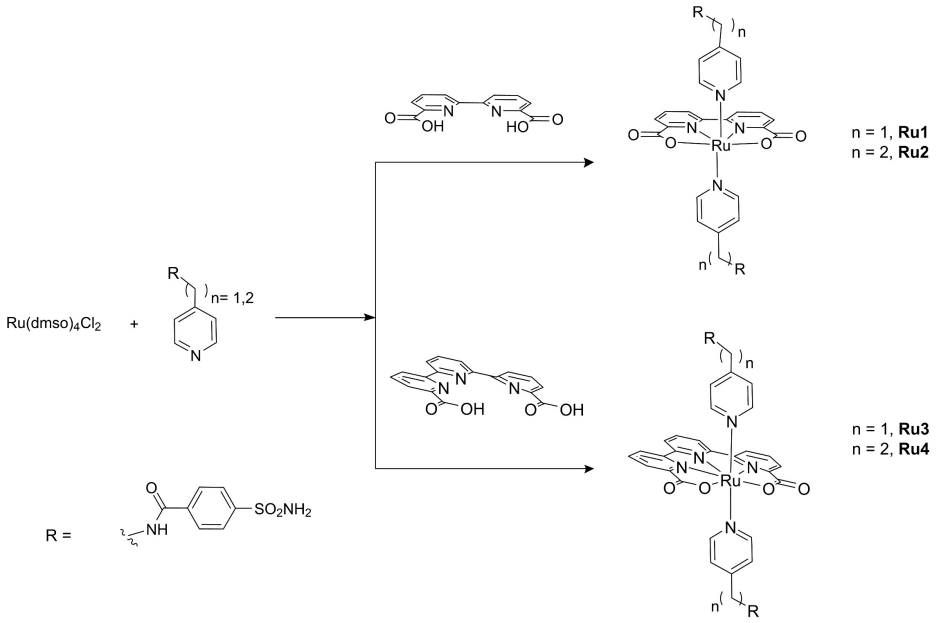


**Figure 4.2.** Formula and synthesis of ruthenium complexes **Ru1**-**Ru4**.

### 4.2.2 Preparation and characterization of the artificial carbonic anhydrase – ruthenium adducts

To prepare the targeted artificial carbonic anhydrases the interaction between the complexes and the protein was studied first by gel electrophoresis using a 15% acrylamide gel. Commercial bovine carbonic anhydrase was incubated with **Ru1** in two BCA:Ru1 ratio (20:10 and 20:200 μM) using different buffers at 80 mM: phosphate pH 7.5 and 8.0, HEPES pH 7.5, Tris-HCl pH 7.5 and 8.0, and $NaBO_3$ pH 9.0. When a lower concentration of the catalyst was used compared with that of the protein (protein:catalyst 20:10 μM) gel electrophoresis revealed new bands with higher molecular weight than the **BCA** band (Figure AIII.1). When the concentration of the catalyst was increased to 200 μM new bands with molecular weight similar and lower to BCA were visible (~30 kDa). While there was no clear difference

between the reaction in the different buffers used, a clear interaction was observed between **Ru1** and **BCA.**

In a second step, ICP-MS was used to characterize the **BCA:Ru1** adduct. A set of samples containing **BCA** and **Ru1** were incubated in a phosphate buffer using different protein:complex ratios from 0.5:1 to 1:5 μM (Figure AIII.2). After incubation for ~18-20 h, each sample was passed onto a Bio-Rad p6 Spin column to remove any unbound small-molecule ruthenium complex, and the columned solution was prepared for ICP-MS analysis to measure the concentration of Zn and Ru. The results showed that as the concentration of the catalyst rose, the Ru:Zn ratio increased and hence that the concentration of Ru catalyst bound to Zn protein increased a well. The same trend was observed with all the other complexes **Ru2**, **Ru3** and **Ru4**. It was hence hypothesized that the binding site of the Ru complexes was the $Zn^{2+}$-based catalytic center of the protein. Samples of ***apo*BCA** were then produced, *i.e.*, deprived of zinc, following reported experimental procedure based on bis-picolinic acid (BPA) at pH 5.5 in acetate buffer.[17] When ***apo*BCA** was incubated with an excess of **Ru1** (5 fold) overnight at room temperature in the dark, and following purification with a Bio-Rad Spin p6 column as above, ICP-MS revealed that the concentration of ruthenium in the protein after incubation, was the same compared to negative control. This result strongly indicated that the Ru complexes bound selectively to the protein's natural $Zn^{2+}$ cofactor.

We then calculated the dissociation constant of each ligand and complex with the **BCA** protein. The affinity of a sulfonamide-functionalized molecule towards **BCA** can be analysed using a dansylamide-based fluorescence competitive assay, (for dansylamide (**DNSA**) **competitive assay**, see Experimental section 4.5.6). This fluorophore is quenched in water but becomes strongly emissive once bound to the protein. Displacement by a competitor such as **L1** or **L2** lowers the emission of dansylamide, which allows to measure dissociation constants (Figure AIII.3 and AIII.4). The binding measurements demonstrated a good affinity of the linker **L1** and **L2** with the protein, with dissociation constant ($K_d$) values of 17 and

84 nM, respectively (Table 4.1, Entry 1 and 2). Those values are similar to those reported for other aryl-sulfonamides compounds.[2] For the complexes **Ru1**-**Ru4** a similar trend in binding strength was found (Figure AIII.6 to AIII.9). For the complexes **Ru2** and **Ru4** with a longer linker **L2** the dissociation constant, $K_d$, was higher than for those (**Ru1** and **Ru3**) based on **L1** (Table 4.1). In addition, for the bda-based complexes **Ru1** and **Ru2**, $K_d$ was lower than for the tpyda-based complexes **Ru3** and **Ru4**. The $K_d$ ratio between **Ru1** and **Ru2 (**0.66) was quite similar as the one between **Ru3** and **Ru4** (0.63). These results suggested that besides the length of the linker, the different sizes of the complexes also brought some limitation for the binding of the complex to the protein catalytic pocket.

**Table 4.1.** Dissociation constant ($K_d$, nM) of linkers **L1**-**L2** and ruthenium complexes **Ru1**-**Ru4** towards **BCA**.

| Entry | Sample | Dissociation constant, $K_d$ (nM) |
|---|---|---|
| 1 | **L1** | (17 ± 2) |
| 2 | **L2** | (84 ± 14) |
| 3 | **Ru1** | (66 ± 11) |
| 4 | **Ru2** | (100 ± 23) |
| 5 | **Ru3** | (127 ± 28) |
| 6 | **Ru4** | (201 ± 24) |

*DNSA was used as reference for the calculations of $K_d$.

UV-vis and circular dichroism (CD) were then used to further interrogate the interaction between the Ru complexes and **BCA**. UV-vis showed a blue shift of the d-d band of the complexes **Ru1** and **Ru2** from 390 nm in the free complexes to ~350 nm once bound to the protein (Figure AIII.10). For **Ru3** and **Ru4** the shift of the d-d band was not significant, but a new band at 320 nm became visible upon interacting with **BCA**, probably characteristic for the terpyridine moiety. For all four ArM with **BCA-Ru1** to **BCA-Ru4**, a new band at 480 nm appeared upon binding of the ruthenium complexes to the protein, which was characteristic of the metal-to-ligand

charge transfer (MLCT) transition of the complexes. The CD spectra showed a more surprising result (Figure AIII.11): for **BCA-Ru1**, there was no significant change of the conformation of the protein, while for **BCA-Ru2**, **BCA-Ru3** and **BCA-Ru4** the binding of the metal complex to BCA did affect significantly the secondary structure of the protein, notably around 215 and 225 nm, which are related to the antiparallel β-sheet and α-helix domains of **BCA**.[5] Overall, all the synthesized complexes showed a positive interaction with BCA but **Ru1** had the best complex-protein interaction with **BCA** in the studied conditions, thus was our best candidate to be tested for WO.

### 4.2.3. Photocatalysis

Photocatalytic water oxidation was tested for all four **BCA-Ru** conjugates, and compared to that of the free **Ru1**-**Ru4** complexes, in presence of $[Ru(bpy)_3](ClO_4)_2$ as photosensitizer (PS, 0.3 mM) and $Na_2S_2O_8$ as sacrificial electron acceptor (SA, 5 mM). To start with, the effect of catalyst concentration on the photocatalytic activity of the enzyme-free system was studied with free **Ru1**. Upon decreasing the concentration of **Ru1** from 50 to 5 μM (Table 4.2), the activity of the photocatalytic system, expressed in turnover number at 60 min (TON), increased, to culminate at a concentration of 5 μM (TON = 36, Entry 5 in Table 4.2). At this concentration the catalyst was still active after 200 min irradiation, which was not observed at different concentrations. Surprisingly, **Ru1** was found to be the only free ruthenium complex to be active under these conditions. As control experiments with **BCA-Ru** catalysts, an experiment with 50 μM free **Ru1** in presence of 50 μM of added $Zn(OAc)_2$ produced a comparable amount of dioxygen to that obtained in absence of zinc. Thus, $Zn^{2+}$ ions do not interfere in the photocatalytic process.

**Table 4.2.** Optimization of $O_2$ evolution for photocatalytic water oxidation using **Ru1** as catalyst.[a]

| Entry | Ru1 concentration (μM) | $O_2$ produce (μmol) | TON | $TOF_{Max}$** |
|---|---|---|---|---|
| 1 | **50** | 0.40±0.07 | 2.3±0.5 | 0.03 |
| 2 | **50*** | 0.36±0.02 | 2.1±0.1 | 0.03 |
| 3 | **25** | 0.67±0.21 | 7.6±2.4 | 0.02 |
| 4 | **10** | 0.82±0.29 | 23±8 | 0.02 |
| 5 | **5** | 0.63±0.23 | 36±13 | 0.02 |

[a] **Conditions:** $[Ru(bpy)_3](ClO_4)_2$ = 0.3 mM, $[Na_2S_2O_8]$ = 5 mM, phosphate buffer pH 7.5 (80mM), 450 nm LED (19 mW), 25 ºC, total irradiation time 60 min. $TON_{60min}$ = [$O_2$ μmol produced]/[μmol catalyst]. *$Zn(OAc)_2$ was used in a 50 μM concentration. **Calculated according to the literature,[18] see Experimental section. Experiments were done in *duplo*. For raw data, see Appendix III.25.

The artificial **BCA-Ru** metalloenzymes were then evaluated as water oxidation catalysts in the same photocatalytic conditions as above. First, upon starting to irradiate a sample containing **BCA-Ru1** with blue light (450 nm), $O_2$ evolution was observed, demonstrating the catalytic activity of the artificial metalloenzyme (red trace, Figure 4.3). The presence of the **BCA** protein scaffold led to an increase of the activity by almost 3 times of **BCA-Ru1** compared to **Ru1** (4.64 ± 0.27 μmol *vs*.1.4 ± 0.65 μmol $O_2$ after 200 min, respectively). This corresponded to a remarkable increase in stability of the catalyst, as the TON increased from 80 with the free catalyst **Ru1** to 265 when it was placed is in the enzyme pocket. In addition, the $TOF_{max}$ and $O_2$ generation quantum yields also increased by a 4-fold factor, compared to the free complex **Ru1** as catalyst (Table AIII.1). A control experiment with **BCA-Ru1** in presence of $[Ru(bpy)_3](ClO_4)_2$ and $[Na_2S_2O_8]$ but without light, showed no $O_2$ production (black trace in Figure 4.3), demonstrating that the process was photocatalytic. The BCA enzyme environment activated the ruthenium complex **Ru2** as well, as the artificial metalloenzyme **BCA-Ru2** showed a significantly higher photocatalytic $O_2$ evolution (1.83 ± 0.27 μmol $O_2$, TON 105) compared with free catalyst **Ru2**, which was inactive in such conditions.

Surprisingly, both other artificial metalloenzymes, **BCA-Ru3** and **BCA-Ru4**, showed no oxygen evolution in the same photocatalytic conditions (Table AIII.1). As a control, photocatalysis using **BCA** alone (*i.e.*, without any Ru complex, Figure 4.3) showed no $O_2$ evolution either, which demonstrated the absence of catalytic activity of the protein itself. Overall, these results showed the important role of both the protein scaffold and the structure of the ruthenium water oxidation catalyst on the water oxidation catalytic activity of the **BCA-Ru** artificial metalloenzymes in photocatalytic conditions.

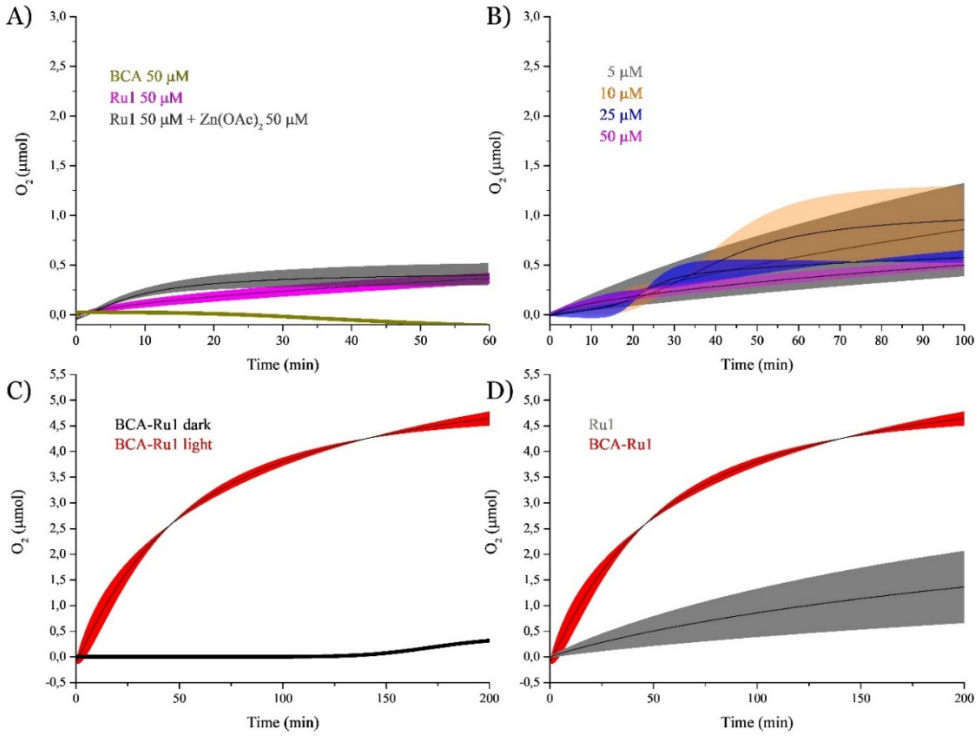


**Figure 4.3.** $O_2$ evolution of **Ru1** and **BCA-Ru1** under photocatalytic conditions. (**A**) Ruthenium-free **BCA** enzyme (50 µM), and enzyme-free catalyst **Ru1** in absence and presence of $Zn(OAc)_2$ (50 µM). (**B**) Photocatalytic activity of free catalyst **Ru1** in different concentrations (<5% DMF was added to dissolve the catalyst). (**C**) Activity of artificial metalloenzyme **BCA-Ru1** (5 µM) as catalyst in the dark and under blue light irradiation. (**D**) Effect of protein scaffold on activity of free **Ru1** and **BCA-Ru1** (5 µM). Conditions**:** $[Ru(bpy)_3](ClO_4)_2$ = 0.3 mM, $[Na_2S_2O_8]$ = 5 mM, phosphate buffer pH 7.5 (80 mM),

blue light (450 nm, 19 mW), 25 °C. Data was fitted with OriginPro software using Hill function. Coloured area represents error (standard deviation) over two independent experiments.

### 4.2.4. Photostability

The activity or lack of activity of a **BCA-Ru** artificial metalloenzyme might depend on its stability in photocatalytic conditions. To study this, we first looked at the behaviour of the free ruthenium catalysts under light irradiation, starting with **Ru1**. A 100 μM solution of **Ru1** in DMF was prepared and irradiated using different light sources (450 nm, 528 nm, 650 nm), following the UV-vis spectrum of the solution *vs.* irradiation time (Figure AIII.19). When irradiated with blue or green light in such conditions **Ru1** was photostable for at least 3 h. When the light source was changed to red (650 nm), a new absorption band appeared at ~700 nm upon irradiation (Figure 4.4A). A similar experiment was performed in DMSO solution to discard any influence of the solvent; the same results were obtained as compared with DMF (Figure AIII.19C). To better understand this result, a sample of **Ru1** in DMSO-*d6* was irradiated with red light and followed by $^{1}$H-NMR. After 3 h irradiation, the spectra of the solution showed the formation of free ligand **L1** characterized for example by the peak at δ = 8.5 ppm (Figure 4.4B). The free complex **Ru1** decomposes hence *via* photosubstitution of the axial pyridyl ligand. In addition, exposing the complex to air produced a visible change of the colour of the solution from dark brown to green. According to UV-vis **Ru4** was also photounstable upon irradiation with blue light, as shown by the changes of the d-d transitions of the complex (350-400 nm, Figure AIII.20). The $^{1}$H-NMR spectra of **Ru4** after blue light irradiation in DMSO-*d6* confirmed photodecomposition of the complex, but without formation of the free ligand **L2** (Figure AIII.17). Unlike the three other complexes, the evolution of the NMR spectra of **Ru3** under blue light irradiation (Figure AIII.16) suggested that the complex was photostable, as neither free ligand **L1** nor decomposition was observed after 180 min irradiation. However, the evolution of the UV-vis spectrum of **Ru3** under blue light irradiation in DMSO showed some

variations reminiscent to that observed with **Ru4** (350-400 nm, Figure AIII.20). Free **Ru2** was the most photostable of the four complexes under blue light irradiation, as neither its UV-vis nor its $^{1}$H-NMR spectra changed upon blue light irradiation (Figure AIII.15 and III.20). Overall, the free ruthenium complexes showed variable photostability under visible light irradiation, from full photostability for **Ru2** to wavelength-dependent photosubstitution reactions of the axial pyridine ligands for **Ru1**.

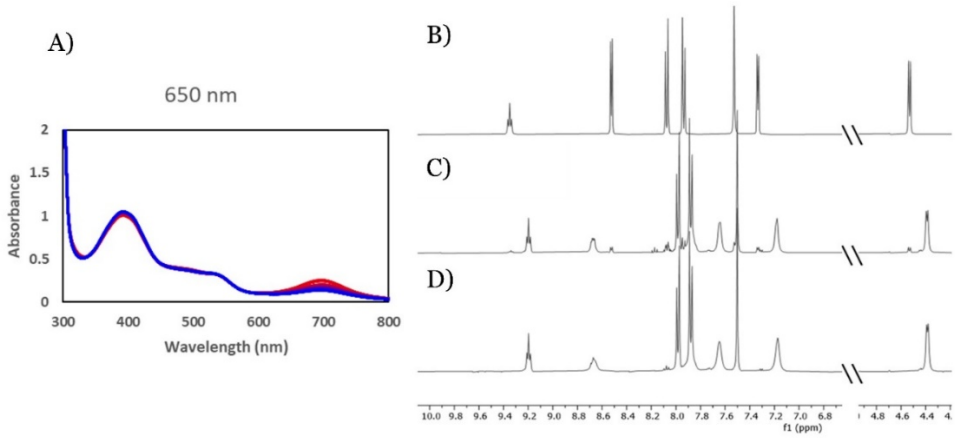


**Figure 4.4.** Stability of **Ru1** under light irradiation. (**A**) Evolution of the UV-vis spectrum of **Ru1** irradiated with red light in DMF (650 nm, 1.6 mW). Evolution of the $^{1}$H-NMR spectrum of **Ru1** irradiated by red light (645 nm) in DMSO-*d6:* (**B**) Reference $^{1}$H-NMR spectrum of sulfonamide linker **L1**; (**C**) $^{1}$H-NMR spectrum of **Ru1** after light irradiation; (**D**) $^{1}$H-NMR spectrum of **Ru1** before light irradiation. [**Ru1**] = 100 μM, 298 K, 3 h.

The effect of **BCA** conjugation on the photostability of the ruthenium complexes was also studied for the four **BCA-Ru** conjugates. UV-vis spectroscopy was used to follow the evolution of the spectra of **BCA-Ru** systems under blue light irradiation in a phosphate buffer solution at pH 7.5 (Figure AIII.21). Like for their enzyme-free analogues, **BCA-Ru1** and **BCA-Ru2** were found photostable under these conditions. Interestingly, for **BCA-Ru3** and **BCA-Ru4** as well no change was visible in the UV-vis spectrum upon blue light irradiation, while **Ru3** and **Ru4** were

unstable in such conditions. These observations supported the hypothesis that the interaction between the catalyst and the enzyme stabilized the ruthenium complexes, notably against ligand photodissociation.

Finally, the fate of the artificial metalloenzyme in photocatalytic conditions was investigated by measuring the ESI mass spectrum of a sample of **BCA-Ru1** in presence of the photosensitizer and the electron acceptor, before and after 3 h blue light irradiation. Before irradiation, the signal corresponding to the protein (*m* = 29027 Da) was clearly found in the mass spectra (Figure AIII.30). However, after irradiation the spectra did not show any peak corresponding to the initial state of the protein. Instead, other signals such as m = 29265 Da and 56190 Da, were observed that could be related with an oxidized form of the protein, as results of oxidation with $^1O_2$ generated from $O_2$ via photocatalysis (Figure AIII.31). SDS-gel electrophoresis analysis was realized on the sample following photocatalysis, but it was impossible to visualize any band corresponding to **BCA**. To investigate in more details what happens during photocatalysis, size exclusion chromatography multi-angle light scattering (SEC-MALS) and dynamic light scattering (DLS) were used (Figure 4.5). According to SEC-MALS, before photocatalysis both **BCA-Ru1** alone and **BCA-Ru1** in the photocatalytic mixture have the same protein distribution pattern, with the monomer as most abundant species (retention volume ~ 16 mL), and a small percentage of the dimer (retention volume ~14 mL) and trimer (retention volume ~ 13 mL, Figure 4.5A). After light irradiation of **BCA-Ru1** in the photocatalytic mixture, a broader band was observed, displaced to the region of the dimeric form of the protein; however, the mass calculated for this signal is lower than the monomer of the protein (~26760 Da, Figure AIII.29). This result indicated that the protein scaffold changed during photocatalysis, making it more hydrophilic, changing the global charge and reducing the interaction with the Superdex column of the SEC-MALS apparatus or breaking down the protein partially. DLS revealed no significant changes in the size of both protein alone and the protein in the photocatalytic mixture before light irradiation (~1-2 nm), yet the sample after

photocatalysis showed particles approximately twice of the size present in the sample (~3 nm)(Figure 4.5B). These results indicated that the protein significantly changed its tertiary or quaternary structure during photocatalysis.

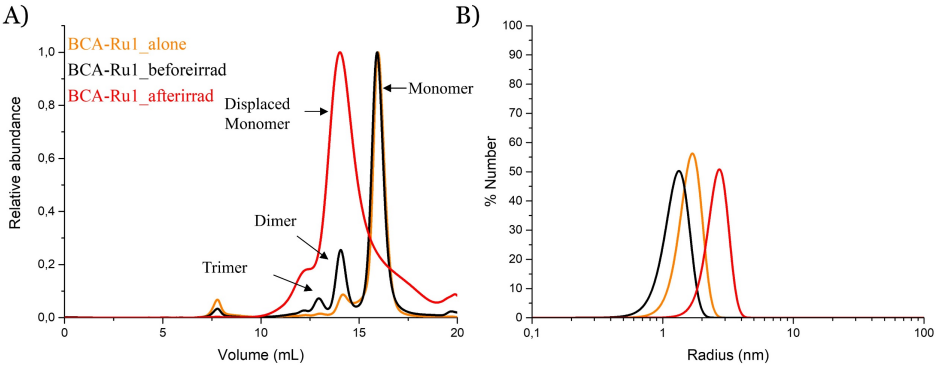


**Figure 4.5.** Aggregation study of **BCA-Ru1** in water oxidation photocatalytic conditions. SEC-MALS trace (**A**) and DLS size distribution (**B**) of a **BCA-Ru1** aqueous solution before (orange, artificial enzyme alone, and black, artificial enzyme in presence of photosensitizer and electron acceptor) and after light irradiation (red, in photocatalytic mixture). Conditions: $[Ru(bpy)_3](ClO_4)_2$= 0.3 mM, $[Na_2S_2O_8]$ = 5 mM, [**BCA-Ru**] = 5 μM, phosphate buffer pH 7.5 (80 mM), 450 nm LED (19 mW), 25 ºC. For DLS, the samples were measured in the irradiation buffer. For SEC-MALS, the samples were run with a phosphate buffer pH 7.0 (50 mM) + NaCl (100 mM).

### 4.2.5. Effects of pH on photocatalysis

Given that the structure and activity of enzymes are often pH-dependent, we studied the influence of pH on the photocatalytic $O_2$ evolution of the most active artificial metalloenzyme, **BCA-Ru1 (**Figure 4.6A*)*. This system was found the most active at pH 6.5 and the least active at pH 8.0 and 5.5, giving increasing TON in the order 8.0 ~5.5 < 7.5~9.0 < 6.5 (Table AIII2). This result showed the versatility of artificial enzymes, which can catalyse the reaction at different pH's and at low concentrations (5 μM). At pH 5.5 the low photocatalytic activity was accompanied by the formation of a precipitate. The precipitate and the solution were both analysed by ICP-MS; Zn was not found in the solution, but in the solid together with Ru. We hypothesize that at such low pH Zn may dissociate from the pocket of the **BCA**

enzyme and precipitate together with the catalyst **Ru1**, which could explain the low activity of the system. It is interesting to note that the stability was the highest at pH 6.5 (followed by pH 9.0), while pH 7.5 is the optimum for the natural catalytic activity of the **BCA** enzyme, *i.e.*, $CO_2$ hydration. In addition, an opposite trend was observed for **BCA-Ru2**, where the activity of the photocatalytic system increased with pH: the highest TON (279) was found at pH 9.0 and the lowest at pH 6.5 (TON 73) (Figure 4.6B, Table AIII3). These results indicated that the length of the linkers had a significant influence on the location, activity, and/or stability, of the catalyst in the catalytic pocket of the **BCA** enzyme.

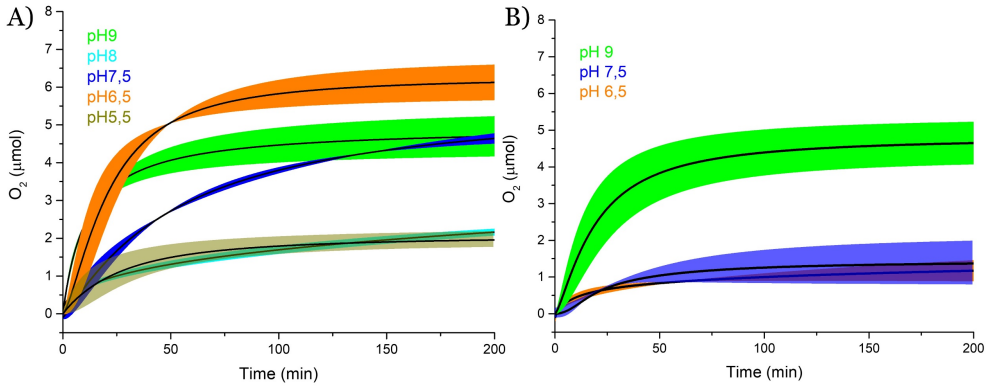


**Figure 4.6.** Photocatalytic $O_2$ evolution reaction catalysed by **BCA-Ru1** (**A**) and **BCA-Ru2** (**B**) at different pH. For pH 6.5 until pH 8.0, a phosphate buffer was used. For pH 9.0, a borate buffer was used; and for pH 5.5 and acetate buffer was used. All buffers had a concentration of 80 mM. Conditions: $[Ru(bpy)_3](ClO_4)_2$= 0.3 mM, $[Na_2S_2O_8]$ = 5 mM, [**BCA-Ru**] = 5 µM, blue light (450 nm, 19 mW), 25 ºC. The original data were averaged and fitted with OriginPro software using Hill function represented in the plot as black line, and the error (standard deviation) is represented in colour, calculated over 2 independent experiments. For raw data, see Figure AIII.27 and III.28.

### 4.3. Discussion

The binding strength between the **BCA** protein and the ruthenium-based catalysts **Ru1-Ru4** are, according to our measurements, comparable with that of other reported small molecules binding to **BCA** *via* sulfonamides.[2] However, **L1** and **Ru1** were shown to have a better affinity with **BCA** than **L2** and **Ru2**, respectively.

As the ligands binding to zinc are identical, these differences must be related to the environment provided around the ruthenium complex by the protein, which is sometimes called the "second coordination sphere". The interaction between the complex and the residues that surround the binding pocket will depend on the length of the linker between the pyridine and sulfonamide ligands, as well as the affinity of the molecule as a whole for the hydrophobic or hydrophilic regions of the binding pocket (Figure 4.7B). The $bda^{2-}$ and $tpyda^{2-}$ equatorial ligands also influence the interaction between the ruthenium compound and the protein (Figure 4.7C). $Tpyda^{2-}$ is larger than $bda^{2-}$, which may generate significant steric hindrance with the protein scaffold in the case of **Ru3** and **Ru4** complexes. In addition, these $tpyda^{2-}$ complexes are in a dynamic equilibrium, as the negative charges of the carboxylate groups cannot bind simultaneously to ruthenium, which is reported to be vital in the catalytic cycle of this compounds (Figure 4.7A).[16,19] This process might generate some form of electrostatic interaction with a residue in the pocket of **BCA**, which may be detrimental to the catalytic activity of **BCA-Ru3** and **BCA-Ru4**. Such effect is not occurring for the **Ru1** and **Ru2** complexes bearing $bda^{2-}$, where both carboxylates remain bound to ruthenium throughout the catalytic cycle.[20] This hypothesis is supported by the $K_d$ values for **Ru3** and **Ru4**, which are the double of those for **Ru1** and **Ru2**, respectively, showing weaker binding.

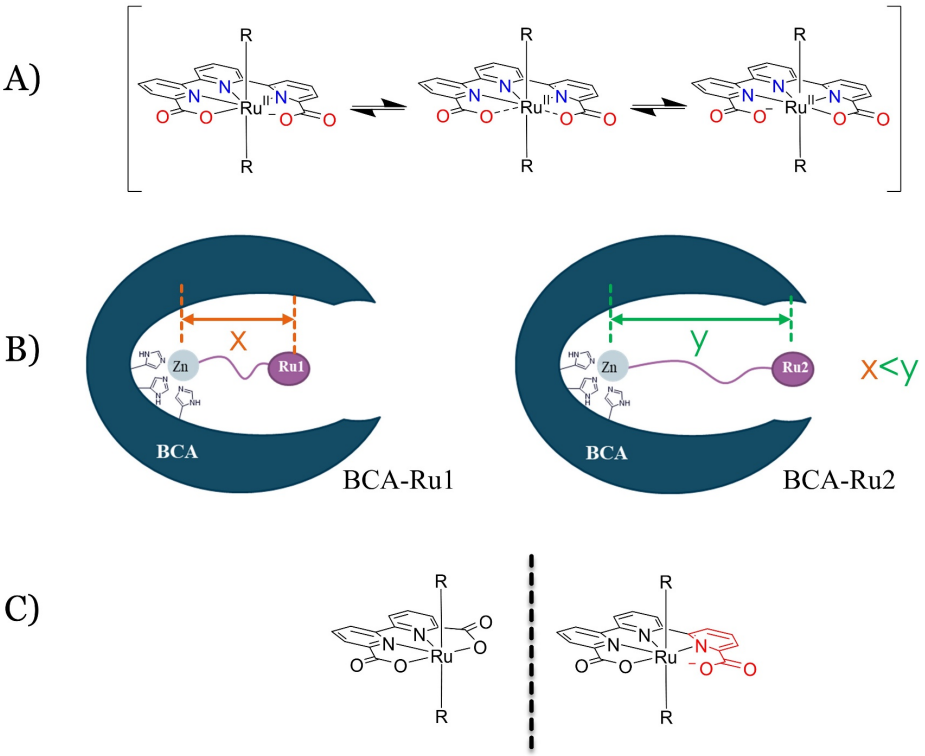


**Figure 4.7.** (**A**) Resonance of negative charge of oxygen the carboxylate group of $tpdya^{2-}$ bearing complexes.[19] (**B**) Graphic representation of the position of **Ru1** and **Ru2** once bound to the protein pocket. (**C**) Structural differences between ruthenium complexes based on the $bda^{2-}$ or $tpyda^{2-}$ ligands.

The strong binding of **Ru1-Ru4** to **BCA** provided a unique opportunity to study the water oxidation properties of the **BCA-Ru** artificial enzymes in photocatalytic conditions. According to our data, binding of the ruthenium complexes to **BCA** is a versatile method to solubilize them in aqueous solution without the need for using any organic solvent. Acetonitrile, for example, is typically used for dissolving [Ru(bda)(picoline)$_2$]-like water oxidation catalysts (WOC) in aqueous solutions; however, the excellent coordination properties of MeCN make its role in the catalytic cycle of the reaction to this day not fully understood.[21] Next to providing a general scaffold for solubilization in water, **BCA** also increased the catalytic properties of the ruthenium catalyst in a structure-dependent manner, as

only **Ru1** and **Ru2** were catalytically active and showed different catalytic properties. As described above, the binding of **Ru1** to **BCA** increased not only the stability (TON) but also the activity (TOF) of the photocatalytic system, reaching TON of 348 comparable to or higher than that reported for ruthenium-based water oxidation catalysts in similar photochemical conditions (*i.e.* [Ru(bda)(4-bromopyridine)$_2$], [Ru(bda)(4-picoline)$_2$] and [Ru(bda)(isoquinoline)$_2$] with TON of 251, 100 and 217, respectively).[21–24] Like **Ru1**, **Ru2** became active once inside the enzyme pocket, while its activity was negligible when it was used as free catalyst in otherwise identical conditions. Most probably, one of the reasons for this lack of activity of free **Ru1** and **Ru2** is the concentration of the catalyst chosen for this photocatalytic system, which was much lower (5 μM) than in previous reports (10 to 80 μM).[13,21] In addition, in absence of an enzyme support DMF was required in the catalytic mixture to solubilize the complexes in water, which might induce the formation of catalytically inactive carbonyl ruthenium species *via* photocatalytic decomposition of DMF into CO and dimethylamine.[25] In terms of stability, several of the enzyme-free ruthenium-based water oxidation catalysts included in this study were unstable under visible light irradiation, while after conjugation with **BCA** they became photostable. Complex **Ru1**, in particular, showed wavelength-dependent pyridine ligand photodissociation, which may lead in near-neutral pH aqueous solutions to the formation of a catalytically inactive dimer or trimer of the Ru complex, as described by Sun *et al*.[20,26,27] The terpyridine-based complexes **Ru3** and **Ru4,** on the other hand, were coordinatively unstable under blue light irradiation. The incorporation of all four Ru complexes into the protein scaffold led to light-stable complexes, which is critical for photocatalysis.

Given that the photocatalysis was performed using low concentrations of the artificial water-oxidizing metalloenzyme, we hypothesize that the mechanism of **BCA-Ru1** for water oxidation is probably mononuclear, as reported for similar ruthenium complexes.[24] The presumable location of the complex in the pocket of the

enzyme and the size of the enzyme itself may indeed restrict the approach of a second molecule of **BCA-Ru1**, which should decrease the rate of the dinuclear mechanism for WO. In addition, we observed that a closer distance between the complex and the zinc binding site of **BCA** increased the activity of the [Ru(bda)(picoline)$_2$] catalyst at pH 6.5 (**BCA-Ru1** had a better performance than **BCA-Ru2**), while at pH 9.0 the water oxidation activity of both artificial metalloenzymes were similar. These results suggest that the immediate environment, or second coordination sphere of the Ru(bda) catalyst may be different in **BCA-Ru1** and **BCA-Ru2**. At basic pH the mechanism for $O_2$ evolution of both system is probably affected in a similar way by the different environments of the ruthenium catalyst, but at more acidic pH the different aminoacid residues near ruthenium in the binding pocket may have a greater influence on the $O_2$ evolution mechanism, as reported elsewhere.[28,29]

### 4.4. Conclusions

To our knowledge we report here the first ruthenium-based artificial metalloenzyme that can drive photocatalytic $O_2$ evolution *via* water oxidation. The **BCA** protein scaffold proved to be an ideal host for a sulfonamide-functionalized ruthenium catalyst, acting as a support capable to solubilize the hydrophobic complex in purely aqueous buffers, but also improving the activity and stability of the complex, to reach TON of 348 and TOF of 0.31 $min^{-1}$ at exceptionally low catalyst concentration (5 μM). Though the detailed (photo)catalytic mechanism of the **BCA-Ru1** and **BCA-Ru2** systems needs to be further investigated, two new aryl-sulfonamide linkers with high affinity toward **BCA** have been developed, which opens a window for the future development of new **BCA-WOC** systems. Overall, the use of an ArM for catalysing water oxidation brings us closer to biomimicking the natural photosynthesis process.

## 4.5. Experimental section

### 4.5.1. General information

All used chemicals were purchased from Sigma-Aldrich/Merck and used without further purification, unless stated otherwise. $[Ru(bpy)_3](ClO_4)_2$ was synthetized following reported procedure.[30] Bovine carbonic anhydrase was obtained from Sigma Aldrich (C3934). Extent of reaction was monitored using silica-coated aluminium TLC plates. $^1$H-NMR and $^{13}$C-NMR data were recorded on a Bruker Ultrashield 400 MHz for $^1$H-NMR. For all NMR spectra in this work, DMSO-*d6* was used as deuterated solvent. Chemical shifts are reported in ppm and relative to DMSO (δ = 2.50 ppm). Methanol was dried using 4Å activated molecular sieves (heated for 3 days in an oven at 150 ºC). (Semi-native) Gel electrophoresis was performed using 15 % polyacrylamide gels containing 0.1 % sodium dodecyl sulphate (SDS).[31]

### 4.5.2. Synthesis of 4-(aryl-sulfonamide)-pyridines linkers, L1 and L2

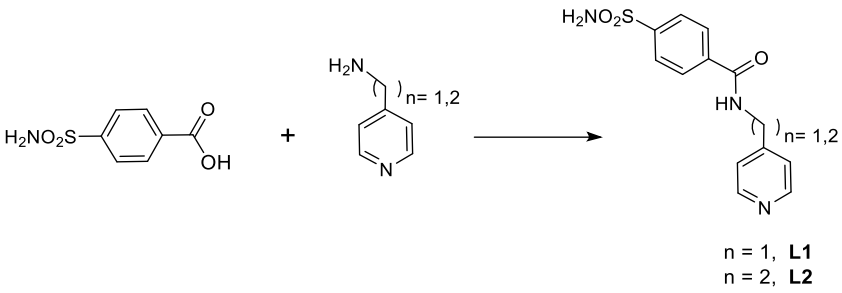


The procedure for ligand synthesis was based on a reported procedure by Roy et al. that was adjusted to synthesise the novel compounds **L1** and **L2**.[14] 4-sulfamoylbenzoic acid (1.00 g, 4.99 mmol, 1 eq) was dissolved in a mixture of DCM (25 mL) and triethylamine (2.08 mL, 14.92 mmol, 3 eq). The desired amine was added to the mixture (4.99 mmol, 1 eq), after which Benzotriazole-1-yloxytris(dimethylamino)phosphonium hexafluorophosphate (BOP) reagent was added (2.20 g, 4.99 mmol, 1 eq). The reaction was stirred for 24 h at room

temperature and quenched with brine (50 mL). Work-up was done by washing the crude precipitate with brine (100 mL), methanol(50 mL x 2), and ethyl acetate (50 mL x 2).

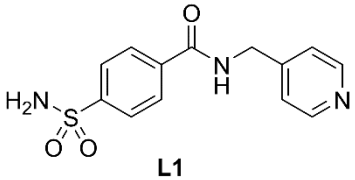


**L1**

Ligand **L1** was prepared according to the general procedure for ligand synthesis. The yield of this amide coupling was 78%.**$^{1}$H NMR (400 MHz, DMSO)** δ 9.35 (t, *J* = 6.0 Hz, 1H, NH), 8.55 – 8.49 (m, 2H, Pyr), 8.07 (d, *J* = 8.5 Hz, 2H, Ar), 7.94 (d, *J* = 8.4 Hz, 2H, Ar), 7.53 (s, 2H, $NH_2$), 7.36 – 7.30 (m, 2H, Pyr), 4.53 (d, *J* = 5.9 Hz, 2H, $CH_2$).**$^{13}$C NMR** δ 166.00 (C=O), 150.06 (Pyr), 148.73 (quaternary), 146.94 (quaternary), 137.36 (quaternary), 128.47 (Ar), 125.64 (Ar), 122.62 (Pyr), 43.00 ($CH_2$). **HRMS [M+H]$^{+}$** calculated mass = 292.07504, detected mass = 292.07484

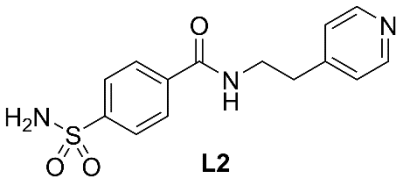


**L2**

Ligand **L2** was prepared according to the general procedure for ligand synthesis. The yield of this amide coupling was 62%. **$^{1}$H NMR (400 MHz, DMSO)** δ 8.80 (t, *J* = 5.5 Hz, 1H, NH), 8.51 – 8.45 (m, 2H, Pyr), 7.98 – 7.93 (m, 2H, Ar), 7.92 – 7.87 (m, 2H, Ar), 7.50 (s, 2H, $NH_2$), 7.31 – 7.25 (m, 2H, Pyr), 3.56 (td, *J* = 7.1, 5.5 Hz, 2H, $CH_2$), 2.90 (t, *J* = 7.1 Hz, 2H, $CH_2$). **$^{13}$C NMR** δ 165.65 (C=O), 149.93 (Pyr), 148.81 (quaternary), 146.67 (quaternary), 138.49 (quaternary), 128.24 (Ar), 126.09 (Ar), 124.73 (Pyr), 40.21 ($CH_2$), 34.53 ($CH_2$). **HRMS [M+H]$^{+}$** calculated mass = 306.09069, detected mass = 306.09050

### 4.5.3. General procedure for the synthesis of Ru1 and Ru2

Precursor complex [Ru(bda)(dmso)$_2$] was prepared according to a procedure published by Yazdani, et al., adjusted for avoiding the use of a glovebox.[32] 6,6'-bipyridine-2,2'-dicarboxylic acid ($H_2$bda, 1 eq) and [Ru(dmso)$_4$Cl$_2$] (1 eq) were added to a round-bottom flask and placed under nitrogen atmosphere. The solids were dissolved in dry methanol (10 mL) and the reaction was refluxed overnight. The reaction mixture was cooled to room temperature, then the solid was filtered and washed with methanol (30 mL x 2) and diethyl ether (20 mL x 3) to yield the precursor [Ru(bda)(dmso)$_2$] as a dark-brown solid (23-49%). Ru(bda)(dmso)$_2$ (91.8 mg, 0.194 mmol, 1 eq) and the desired ligand (0.373 mmol, 2.03 eq) were added to a two-neck round-bottom flask and placed under nitrogen atmosphere. Dry methanol (see general information above), was added (10 mL) and the mixture was refluxed for 24 h, cooled down to room temperature, and the solution was filtered and washed with MeOH (50 mL x 2) and Diethyl Ether (50 mL x 2). The solid was dissolved in the minimum amount of DMF (~3 mL) and passed through a SEC column (Cytiva Sephadex LH-20, 3 x 43 cm) mounted using DMF. The first layer was collected, and the solution was poured into a 500 mL flask with 300 mL of diethyl ether. The mixture was placed at 4 $^{o}$C overnight. The resulting precipitate was collected by filtration and washed with diethyl ether (25 mL x 3). The title compound was dried under vacuum over 3 days.

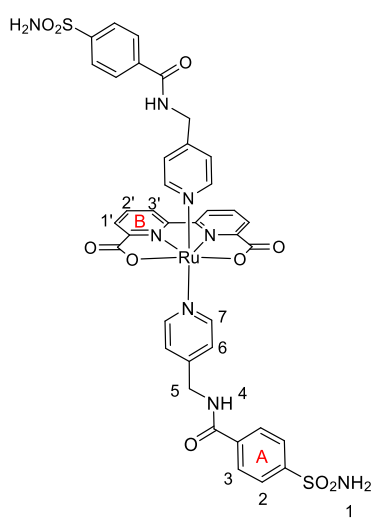


**Ru1. $^{1}$H NMR (400 MHz, DMSO)** δ 9.18 (t, *J* = 5.8 Hz, 2H, NH, A4), 8.67 (d, J = 7.6 Hz, 2H, B1'), 7.97 (d, J = 8.5 Hz, 4H, A7), 7.89 – 7.83 (m, 8H, A6, B2', B3), 7.63 (d, J = 5.9 Hz, 4H, A3), 7.48 (s, 4H, $NH_2$, A1), 7.18 (d, J = 6.0 Hz, 4H, A2), 4.38 (d, J = 5.7 Hz, 4H, $CH_2$, A5).**$^{13}$C NMR (101 MHz, DMSO)** δ 166.00 (C=O), 151.98 (Pyr), 149.82 (quaternary), 146.96 (quaternary), 137.15 (quaternary), 128.52 (Ar), 128.16 (bda), 126.13 (Ar), 125.30 (bda), 123.78 (Pyr), 42.06 ($CH_2$). **HRMS [M+H]$^+$** calculated mass = 927.080, detected mass = 927.079. **Elem. Anal** for $C_{38}H_{32}N_8O_{10}RuS_2$ calculated: C, 49.73; H, 3.85; N, 11.90. Found: C, 49.29; H, 3.48; N, 12.10.

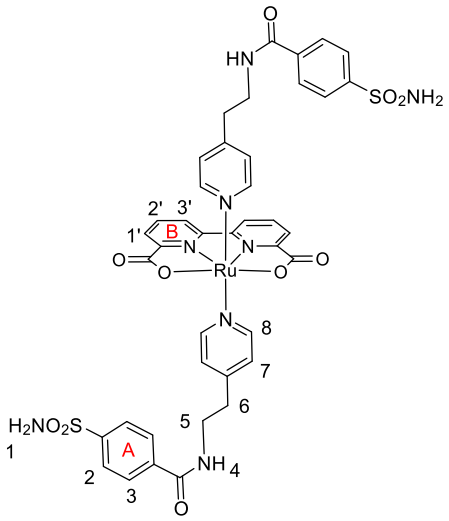


**Ru2. $^{1}$H NMR (400 MHz, DMSO)** δ 8.70 (t, *J* = 5.6 Hz, 2H, NH, A4), 8.65 (dd, *J* = 8.0, 1.2 Hz, 2H, B1'), 7.90 (dd, *J* = 7.6, 1.2 Hz, 4H, A7), 7.96 – 7.79 (m, 8H, A6, B2', B3), 7.57 (d, *J* = 6.4 Hz, 4H, A3), 7.48 (s, 4H, $NH_2$, A1), 7.13 (d, *J* = 6.8 Hz, 4H, A2), 3.32 (4H, $CH_2$, A6), 2.76 (4H, $CH_2$, A5). **$^{13}$C NMR (101 MHz, DMSO)** δ166.00 (C=O), 151.98 (A3), 150.12(quaternary), 147.22 (quaternary), 137.77 (quaternary), 128.23(Ar), 126.07 (Ar), 125.88 (Ar), 125.18 (Ar), 124.30 (B1'), 125.11 (Ar, A2), 39.42 ($CH_2$), 34.26 ($CH_2$). **HRMS [M+H]$^+$** calculated mass

= 955.112, detected mass = 955.111 **Elem. Anal** for $C_{40}H_{36}N_8O_{10}RuS_2$ calculated: C, 50.36; H, 3.80; N, 11.75 . Found: C, 49.68; H, 3.71; N, 11.69.

### 4.5.4. General procedure for the synthesis of Ru3 and Ru4

The complexes were synthetized following a modified procedure reported by Xalas.[33] $[Ru(dmso)_4(Cl)_2]$ (302 mg, 0.622 mmol), [2,2':6',2''-terpyridine]-6,6''-dicarboxylic acid ($H_2$tpyda, 200 mg, 0.622 mmol), and triethylamine (0.6 mL, 4.30 mmol) were degassed in dry methanol (30 mL), refluxed for 10 h, and cooled down to room temperature (RT). A brown solid appeared in the reaction mixture and was filtered, washed with methanol (30 mL x 2) and diethyl ether (20 mL x 3). The solid was dissolved in water (30 mL), and the mixture was heated at 60 °C until the solid had completely dissolved. Then, the solvent was evaporated, and the resulting solid was washed with acetone (100 mL) and diethyl ether (50 mL) and dried under vacuum. In a 100 mL two-neck round-bottom flask [Ru(tpyda)(dmso)($H_2O$)] (100 mg, 0.193 mmol) and the corresponding linker (**L1** or **L2**, 0.4 mmol) were placed. A mixture of solvent MeOH:$H_2O$ 3:2 (20 mL) was degassed and added to the flask dissolving the starting compounds, and the resulting solution was refluxed for 3 days. TLC was performed using DCM/MEOH 5:1 and showed no traces of Ru-complex starting material. The solvent mixture was removed under vacuum and the crude was purified with a SEC column (Cytiva Sephadex LH-20, 3 x 43 cm) mounted using DMF. The first layer was collected and the solution was poured into a 500 mL flask with 300 mL of diethyl ether. The mixture was placed at 4 ºC overnight. The precipitate was collected by filtration and washed with diethyl ether (25 mL x 3). The compound was dried under vacuum over 3 days.

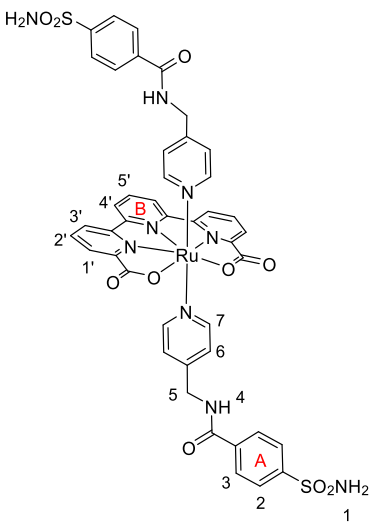


**Ru3. $^{1}$H NMR (400 MHz, DMSO)** δ 9.23 (t, *J* = 5.8 Hz, 2H, NH, A4), 8.70 (d, *J* = 8.1 Hz, 2H, B4'), 8.51 (dd, *J* = 7.9, 1.3 Hz, 2H, B3'), 8.08 (d, *J* = 6.6 Hz , 2H, A3), 8.04 (t, *J* = 8.1 Hz, 1H, B5'), 7.98 (d, *J* = 8.4 Hz, 4H, A6), 7.94 – 7.80 (m, 8H, B1', B2', A7), 7.51 (s, 4H, $NH_2$,A1), 6.99 (d, *J* = 6.4 Hz, 4H, A2), 4.33 (d, *J* = 5.7 Hz, 4H, $CH_2$, A5) **$^{13}$C NMR (101 MHz, DMSO)** δ 169.19 (C=O), 165.94 (quaternary), 161.55 (quaternary), 159.74 (quaternary), 158.43 (quaternary), 152.52 (A3), 150.28, 145.94, 136.24, 128.55 (Ar), 128.72 (B5'), 126.13 (Ar), 123.70 (B4'), 122.06 (A2), 41.13 ($CH_2$). Δ **HRMS $[M+H]^+$** calculated mass = 1004.107, detected mass = 1004.106, **$[M+H]^{2+}$** calculated mass = 502.557, detected mass = 502.556. **Elem. Anal** for $C_{43}H_{36}N_9O_{10}RuS_2$ calculated: C, 51.49; H, 3.52; N, 12.57. Found: C, 51.12; H, 3.60; N, 12.51.

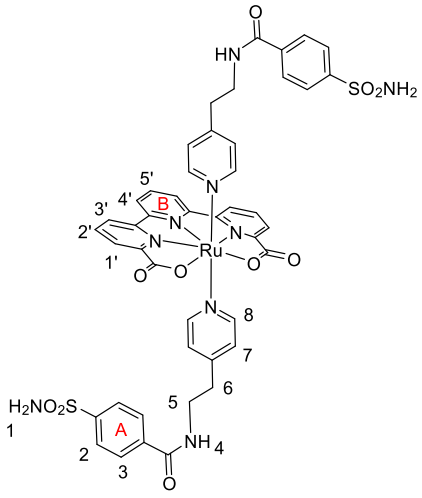


**Ru4. $^{1}$H NMR (400 MHz, DMSO)** δ 8.72 (d, *J* = 8.1 Hz, 2H, B4'), 8.67 (t, *J* = 5.6 Hz, 2H, NH, A4), 8.55 (dd, *J* = 7.7, 1.5 Hz, 2H, B3'), 8.05 (t, *J* = 8.1 Hz, 1H, B5'), 8.01 – 7.89 (m, 8H, B2', B1', A2), 7.85 (d, *J* = 8.6 Hz, 4H, A8), 7.80 (d, *J* = 8.6 Hz, 4H, A7), 7.51 (s, $NH_2$, 4H, A1), 6.99 (d, *J* = 6.8 Hz, 4H, A3) 3.32 (4H, $CH_2$, A6), 2.68 (4H, $CH_2$, A5). **$^{13}$C NMR (101 MHz, DMSO)** δ169.13 (C=O), 165.62 (quaternary), 161.89 (quaternary), 158.00 (quaternary), 152.21 (Ar), 150.00 (quaternary), 146.58 (quaternary), 137.62 (quaternary), 128.14

(A7), 126.41 (Ar), 126.04 (Ar), 125.44 (A8), 124.30 (B1'), 124.69 (Ar, A3), 39.51 ($CH_2$), 34.12 ($CH_2$). Δ **HRMS** $[M+H]^{2+}$ calculated mass = 516.573, detected mass = 516.573 **Elem. Anal** for $C_{45}H_{40}N_9O_{10}RuS_2$ calculated: C, 52.42; H, 3.81; N, 12.23. Found: C, 52.11; H, 3.84; N, 12.07.

### 4.5.5. General procedure for protein-complex screening

A stock solution of the **BCA** protein (30 μM) was prepared in six different buffers at 80 mM concentration: phosphate pH 7.5 and 8.0, HEPES pH 7.5, Tris-HCl pH 7.5 and 8.0, and $NaBO_3$ pH 9.0. Stock solutions of the catalysts were prepared dissolving the catalyst in DMF (1 mM, 1 mL). Protein-catalyst solutions were prepared in a SARSTEDT TC-plate 96 well standard F (ref. 83.3924), adding first the protein solution, where the protein concentration in buffer was fixed at 20 μM and then the catalyst was added directly to the well containing the protein solution in buffer to reach a final volume of 200 μL. The amount of DMF in the solutions was <5% for all the conditions. The catalyst concentration was either 10 μM or 200 μM, depending on the assay. All 96-well plates were incubated overnight (~18-20 h) at room temperature in the dark by covering the plate with aluminium foil. After incubation, gel electrophoresis was run in 15 % polyacrylamide gels containing 0.1 % sodium dodecyl sulphate (semi-native).[31] An aliquot of each sample (10 μL), was mixed with a cracking buffer (10 μL), previously prepared (100% glycerol, bromophenol, 20% 1.0 M tris-HCl pH 8.0) in absence of SDS and β-mercaptoethanol. Gels were loaded with 10 μL of each mixed sample and runned in a running electrophoresis buffer containing 0.1% SDS (Tris base 0.25 M, Glycine 1.9 M) during 50 min at 200 mV.

### 4.5.6. General procedure for artificial BCA-Ru protein formation

A protein solution was prepared weighing the commercially available **BCA** in a Safe-lock tubes 2.0 mL amber Eppendorf (ref. 0030120248) and dissolved in a previously degassed 20 mM phosphate buffer at pH 7.0 (5 mg/mL). The solution was mixed during 15 min at room temperature. A 1 mM complex solution was prepared

in a glass vial (0.5 mL) dissolving it in dry DMF. The different protein:complex mixtures were prepared by adding the amount of complex solution to the protein solution in a 1:5 ratio (excess of complex, keeping a final DMF concentration lower than 5%). Each mixture was mixed overnight at room temperature in a dark Eppendorf. After ~18-20 h incubation time, the sample was concentrated using a Corning concentrator tube 5000 Da MWCO until a small amount of mixture was reached (~2 mL). The sample mixture was then purified using a Hitrap Desalting Column Sigma Aldrich using phosphate buffer (80 mM) at pH 7.5 to remove the excess of the unbound complex. The sample mixture was re-concentrated using a Corning concentrator until reaching a sample volume of 2-2.5 mL. Three 50 µL aliquots of each sample were prepared and analysed by ICP-MS as mentioned above, to determine the concentration of Zn and Ru in each sample. The concentration of protein was then determined using a Bicinchoninic acid kit (BCA protein assay kit) from Bio-Rad (California, USA).

### 4.5.7. Affinity constants determination

The procedure described by Heinisch at al. was used.[34] First, dansylamide (**DNSA)** affinity with the **BCA** protein was calculated. Data was fitted with OriginPro software using the following Equation E1:

$$\boldsymbol{E_{470} = s}\left\{\frac{([\boldsymbol{BCA}]+[\boldsymbol{DNSA}]+\boldsymbol{Kd_{DNSA}})-\sqrt{(([\boldsymbol{BCA}]+[\boldsymbol{DNSA}]+\boldsymbol{Kd_{DNSA}})^2-4[\boldsymbol{BCA}][\boldsymbol{DNSA}])}}{2}\right\} \quad \text{Equation E1}$$

$E_{470}$ is the emission of the mixture at 470 nm, s is the scaling factor, [BCA] is the protein concentration and [DNSA] is the **DNSA** concentration. Second, the affinity of each ruthenium complexes was calculated using Equation E3, derived in the literature:[7]

$$\boldsymbol{r} = \frac{\boldsymbol{F_{obs}-F_{min}}}{\boldsymbol{F_{max}-F_{min}}} \quad \text{Equation E2}$$

$$\text{then, } \boldsymbol{r} = \frac{\mathbf{1}}{\left(\mathbf{1}+\left(\frac{\boldsymbol{Kd_{DNSA}}}{[\boldsymbol{DNSA}]}\right)\left(\mathbf{1}+\left(\frac{[\boldsymbol{catalyst}]}{\boldsymbol{Kd_{catalyst}}}\right)\right)\right)} \qquad \text{Equation E3}$$

Where r is the relative fluorescence $F_{obs}$, $F_{max}$, $F_{min}$, are the fluorescence emission observed, maximum and minimum respectively, [DNSA] is the **DNSA** concentration, $K_d$ is the dissociation constant for DNSA with BCA, [catalyst] is the concentration of the catalyst, $K_{d,catalyst}$ is the dissociation constant for the catalyst.

### 4.5.8. Photostability measured by $^1$H-NMR

NMR light irradiation experiments were performed using a transparent NMR tube. Complex solution was prepared in DMSO-*d6* (~5 mg in 0.6-0.8 mL) and closed tightly. $^1$H-NMR spectrum was measured at t = 0 min (before irradiation) and after 180 min (after irradiation). As irradiation source for blue, red and white light, a 1000 W Xe lamp was used fitted with interference optical filters to select or not the wavelength of irradiation: Schott filter, 5 x 5 cm, 4.5 mm thick, BG7 ($\lambda_{max}$: 488 nm) and RG645 ($\lambda_{max}$: 720 nm) matt glass. The NMR tube was placed in a holder with integrated cooling system, at a distance of 26 cm from the irradiation source, where temperature was set at 25ºC.

### 4.5.9. Photostability measured by UV-vis

Irradiation assays for catalyst complexes were recorded in dry DMF or DMSO as solvents. For the enzyme-complex adducts irradiation assays were recorded using phosphate buffer pH 7.5 (80 mM). The catalysts were added to the cuvette in a 100 μM concentration. Baseline was measured using solvent alone. The first measurement was done before starting irradiation, after which the light was turned on. The light source consisted in a LED fitted to the cuvette via a 1 cm square hole in the LED holder. Each catalyst solution was irradiated with the indicated LED for 3 h (from red to blue) under nitrogen atmosphere, and the absorption spectrum was recorded every minute during irradiation. The power intensity of the LED was set between 18-19 mW using a current of 350 mA, the sample volume was 3 mL, all

samples were degassed with Ar for 30 min prior to irradiation and all experiments were performed under constant stirring.

### 4.5.10. Photocatalytic water oxidation measurements

A 3.5 mL solution in buffer (80 mM) containing 5 μM of the **BCA-Ru** artificial protein, 0.3 mM of the photosensitizer $[Ru(bpy)_3](ClO_4)_2$ and 5 mM of the sacrificial electron acceptor $Na_2S_2O_8$, was placed in a 3.5 mL photoreactor with an integrated water-cooling system settled at 25 $^oC$. The samples were degassed during 30 min with Ar before irradiation. For every dataset, the black line represents the average of two measurements. The coloured traces represent the error (standard deviation) of all the measurements done for each set of data. The average curve of each dataset was plot in using Origin 9.1 software in the following way: Select set of values →Statistics → Descriptive statistics → statistics on Row → Compute Mean. Using the same software, the error was plot using 5% of SD and then corrected with the next script: Statistics → descriptive statistics → statistics on Row → Compute SD. All $O_2$ evolution curves were fitted using software Origin 9.1 in the following way: Analysis → Fitting → Non-linear curve → Growth/Sigmoidal category → Hill1 function. Hill1 function is described as follows Equation E4):

$$y = START + (END - START)\frac{x^n}{(k^n + x^n)} \qquad \text{Equation E4}$$

### 4.5.11. TON, TOF and $O_2$ quantum yield

The turnover number (TON) was calculated using Equation S1 where $n_{O2}$ (μmol) is the number of mol of dioxygen produced by the system during a period of time; $n_{CAT}$ (μmol) is mol of catalyst used in the photocatalytic reaction.

$$TON = \frac{n_{O2}}{n_{CAT}} \qquad \text{Equation E5}$$

Turnover frequency (TOF, $min^{-1}$) was calculated using Equation E6:

$$TOF = \frac{TON}{Irradiation\ time\ (min)} \qquad \text{Equation E6}$$

The $O_2$ production quantum yield was calculated according to Equation E7 as reported in the literature:

$$\varphi = \frac{2n_{CAT}TOF_{max}}{60\Phi(1-10^{-A_e})(\frac{A_{PS}}{A_e})} \qquad \text{Equation E7}$$

where $\eta_{CAT}$ (μmol) is mol of catalyst used in the photocatalytic reaction, Φ (μmol $s^{-1}$) is the photon flux determined by standard ferrioxalate actinometry, $A_e$ is the total absorption of the sample at 450 nm, $A_{PS}$ absorption of the PS in solution at 450 nm, $TOF_{max}$ is the maximum turnover frequency which is calculated according to the literature.[18]

### 4.6. References


(1) Angeli, A.; Carta, F.; Supuran, C. T. Carbonic Anhydrases: Versatile and Useful Biocatalysts in Chemistry and Biochemistry. *Catalysts* **2020**, *10* (9). https://doi.org/10.3390/catal10091008.

(2) Lindskog, S. Structure and Mechanism of Carbonic Anhydrase. *Pharmacology & Therapeutics* **1997**, *74* (1), 1–20. https://doi.org/10.1016/S0163-7258(96)00198-2.

(3) Ferraroni, M.; Cornelio, B.; Sapi, J.; Supuran, C. T.; Scozzafava, A. Sulfonamide Carbonic Anhydrase Inhibitors: Zinc Coordination and Tail Effects Influence Inhibitory Efficacy and Selectivity for Different Isoforms. *Inorganica Chimica Acta* **2018**, *470*, 128–132. https://doi.org/10.1016/j.ica.2017.03.038.

(4) Monnard, F. W.; Heinisch, T.; Nogueira, E. S.; Schirmer, T.; Ward, T. R. Human Carbonic Anhydrase II as a Host for Piano-Stool Complexes Bearing a Sulfonamide Anchor. *Chemical Communications.* **2011**, *47* (29), 8238. https://doi.org/10.1039/c1cc10345h.

(5) Castro, A. M. de; Ferreira, E.; Portugal, C.; Neves, L. A.; Crespo, J. G. Biocatalytic CO2 Absorption and Structural Studies of Carbonic Anhydrase

under Industrially-Relevant Conditions. *International Journal of Molecular Sciences.* **2020**, *21* (8), 2918. https://doi.org/10.3390/ijms21082918.

(6) Fu, Y.; Jiang, Y.-B.; Dunphy, D.; Xiong, H.; Coker, E.; Chou, S. S.; Zhang, H.; Vanegas, J. M.; Croissant, J. G.; Cecchi, J. L.; Rempe, S. B.; Brinker, C. J. Ultra-Thin Enzymatic Liquid Membrane for CO2 Separation and Capture. *Nature Communications.* **2018**, *9* (1), 990. https://doi.org/10.1038/s41467-018-03285-x.

(7) Villarejo, A. A Photosystem II-Associated Carbonic Anhydrase Regulates the Efficiency of Photosynthetic Oxygen Evolution. *The EMBO Journal* **2002**, *21* (8), 1930–1938. https://doi.org/10.1093/emboj/21.8.1930.

(8) Casadevall, C.; Zhang, H.; Chen, S.; Sommer, D. J.; Seo, D.-K.; Ghirlanda, G. Photoelectrochemical Water Oxidation by Cobalt Cytochrome C Integrated-ATO Photoanode. *Catalysts* **2021**, *11* (5), 626. https://doi.org/10.3390/catal11050626.

(9) Abdi, Z.; Bagheri, R.; Song, Z.; Najafpour, M. M. Water Oxidation by Ferritin: A Semi-Natural Electrode. *Scientific Reports.* **2019**, *9* (1), 11499. https://doi.org/10.1038/s41598-019-47661-z.

(10) Olshansky, L.; Huerta-Lavorie, R.; Nguyen, A. I.; Vallapurackal, J.; Furst, A.; Tilley, T. D.; Borovik, A. S. Artificial Metalloproteins Containing $Co_4O_4$ Cubane Active Sites. *Journal of the American Chemical Society.* **2018**, *140* (8), 2739–2742. https://doi.org/10.1021/jacs.7b13052.

(11) Kim, M.-C.; Lee, S.-Y. Catalytic Water Oxidation by Iridium-Modified Carbonic Anhydrase. *Chemistry - An Asian Journal.* **2018**, *13* (3), 334–341. https://doi.org/10.1002/asia.201701543.

(12) Hetterscheid, D. G. H.; Reek, J. N. H. Periodate as an Oxidant for Catalytic Water Oxidation: Oxidation via Electron Transfer or O-Atom Transfer?. *European Journal of Inorganic Chemistry.* **2014**, *2014* (4), 742–749. https://doi.org/10.1002/ejic.201300249.

(13) Duan, L.; Xu, Y.; Zhang, P.; Wang, M.; Sun, L. Visible Light-Driven Water Oxidation by a Molecular Ruthenium Catalyst in Homogeneous System. *Inorganic Chemistry.* **2010**, *49* (1), 209–215. https://doi.org/10.1021/ic9017486.

(14) Roy, B. C.; Banerjee, A. L.; Swanson, M.; Jia, X. G.; Haldar, M. K.; Mallik, S.; Srivastava, D. K. Two-Prong Inhibitors for Human Carbonic Anhydrase II. *Journal of the American Chemical Society.* **2004**, *126* (41), 13206–13207. https://doi.org/10.1021/ja047271k.

(15) Fan, T.; Duan, L.; Huang, P.; Chen, H.; Daniel, Q.; Ahlquist, M. S. G.; Sun, L. The Ru-Tpc Water Oxidation Catalyst and Beyond: Water Nucleophilic Attack Pathway versus Radical Coupling Pathway. *ACS Catalysis.* **2017**, *7* (4), 2956–2966. https://doi.org/10.1021/acscatal.6b03393.

(16) Matheu, R.; Benet-Buchholz, J.; Sala, X.; Llobet, A. Synthesis, Structure, and Redox Properties of a *Trans* -Diaqua Ru Complex That Reaches Seven-Coordination at High Oxidation States. *Inorganic Chemistry.* **2018**, *57* (4), 1757–1765. https://doi.org/10.1021/acs.inorgchem.7b02375.

(17) Kim, J. K.; Lee, C.; Lim, S. W.; Adhikari, A.; Andring, J. T.; McKenna, R.; Ghim, C.-M.; Kim, C. U. Elucidating the Role of Metal Ions in Carbonic Anhydrase Catalysis. *Nature Communications.* **2020**, *11* (1), 4557. https://doi.org/10.1038/s41467-020-18425-5.

(18) Liu, C.; van den Bos, D.; den Hartog, B.; van der Meij, D.; Ramakrishnan, A.; Bonnet, S. Ligand Controls the Activity of Light-Driven Water Oxidation Catalyzed by Nickel(II) Porphyrin Complexes in Neutral Homogeneous Aqueous Solutions. *Angewandte Chemie International Edition* **2021**, *60* (24), 13463–13469. https://doi.org/10.1002/anie.202103157.

(19) Matheu, R.; Ertem, M. Z.; Benet-Buchholz, J.; Coronado, E.; Batista, V. S.; Sala, X.; Llobet, A. Intramolecular Proton Transfer Boosts Water Oxidation Catalyzed by a Ru Complex. *Journal of the American Chemical Society.* **2015**, *137* (33), 10786–10795. https://doi.org/10.1021/jacs.5b06541.

(20) Grądzka-Kurzaj, I.; Gierszewski, M.; Timmer, B. J. J.; Ziółek, M. Molecular Water Oxidation Catalysis: Characterization of Subnanosecond Processes and Ruthenium "Green Dimer" Formation. *ACS Applied Energy Materials.* **2021**, *4* (3), 2440–2450. https://doi.org/10.1021/acsaem.0c02959.

(21) Li, F.; Xu, C.; Wang, X.; Wang, Y.; Du, J.; Sun, L. Visible Light-Driven Oxygen Evolution Using a Binuclear Ru-Bda Catalyst. *Chinese Journal of Catalysis* **2018**, *39* (3), 446–452. https://doi.org/10.1016/S1872-2067(18)63024-4.

(22) Kärkäs, M. D.; Verho, O.; Johnston, E. V.; Åkermark, B. Artificial Photosynthesis: Molecular Systems for Catalytic Water Oxidation. *Chemical Reviews.* **2014**, *114* (24), 11863–12001. https://doi.org/10.1021/cr400572f.

(23) Ye, S.; Ding, C.; Liu, M.; Wang, A.; Huang, Q.; Li, C. Water Oxidation Catalysts for Artificial Photosynthesis. *Advance Materials.* **2019**, *31* (50), 1902069. https://doi.org/10.1002/adma.201902069.

(24) Wang, L.; Duan, L.; Tong, L.; Sun, L. Visible Light-Driven Water Oxidation Catalyzed by Mononuclear Ruthenium Complexes. *Journal of Catalysis* **2013**, *306*, 129–132. https://doi.org/10.1016/j.jcat.2013.06.023.

(25) Kärkäs, M. D.; Åkermark, T.; Chen, H.; Sun, J.; Åkermark, B. A Tailor-Made Molecular Ruthenium Catalyst for the Oxidation of Water and Its Deactivation through Poisoning by Carbon Monoxide. *Angewandte Chemie International Edition* **2013**, *52* (15), 4189–4193. https://doi.org/10.1002/anie.201210226.

(26) Yang, Q.-Q.; Jiang, X.; Yang, B.; Wang, Y.; Tung, C.-H.; Wu, L.-Z. Amphiphilic Oxo-Bridged Ruthenium "Green Dimer" for Water Oxidation. *iScience* **2020**, *23* (3), 100969. https://doi.org/10.1016/j.isci.2020.100969.

(27) Zhang, B.; Li, F.; Zhang, R.; Ma, C.; Chen, L.; Sun, L. Characterization of a Trinuclear Ruthenium Species in Catalytic Water Oxidation by Ru(Bda)(Pic)2 in Neutral Media. *Chemical Communication.* **2016**, *52* (55), 8619–8622. https://doi.org/10.1039/C6CC04003A.

(28) Shaffer, D. W.; Xie, Y.; Szalda, D. J.; Concepcion, J. J. Manipulating the Rate-Limiting Step in Water Oxidation Catalysis by Ruthenium Bipyridine–Dicarboxylate Complexes. *Inorganic Chemistry.* **2016**, *55* (22), 12024–12035. https://doi.org/10.1021/acs.inorgchem.6b02193.

(29) Wang, L.-P.; Wu, Q.; Van Voorhis, T. Acid−Base Mechanism for Ruthenium Water Oxidation Catalysts. *Inorganic Chemistry.* **2010**, *49* (10), 4543–4553. https://doi.org/10.1021/ic100075k.

(30) Fu, S.; Liu, Y.; Ding, Y.; Du, X.; Song, F.; Xiang, R.; Ma, B. A Mononuclear Cobalt Complex with an Organic Ligand Acting as a Precatalyst for Efficient Visible Light-Driven Water Oxidation. *Chem. Commun.* **2014**, *50* (17), 2167–2169. https://doi.org/10.1039/C3CC48059C.

(31) Opdam, L. V.; Polanco, E. A.; de Regt, B.; Lambertina, N.; Bakker, C.; Bonnet, S.; Pandit, A. A Screening Method for Binding Synthetic Metallo-Complexes to Haem Proteins. *Analytical Biochemistry* **2022**, *653*, 114788. https://doi.org/10.1016/j.ab.2022.114788.

(32) Yazdani, S.; Silva, B. E.; Cao, T. C.; Rheingold, A. L.; Grotjahn, D. B. X-Ray Crystallography and Electrochemistry Reveal Electronic and Steric Effects of Phosphine and Phosphite Ligands in Complexes RuII(K4-Bda)(PR3)2 and RuII(K3-Bda)(PR3)3 (Bda = 2,2′-Bipyridine-6,6′-Dicarboxylato). *Polyhedron* **2019**, *161*, 63–70. https://doi.org/10.1016/j.poly.2018.12.033.

(33) Hoque, M. A.; Gil-Sepulcre, M.; de Aguirre, A.; Elemans, J. A. A. W.; Moonshiram, D.; Matheu, R.; Shi, Y.; Benet-Buchholz, J.; Sala, X.; Malfois, M.; Solano, E.; Lim, J.; Garzón-Manjón, A.; Scheu, C.; Lanza, M.; Maseras, F.; Gimbert-Suriñach, C.; Llobet, A. Water Oxidation Electrocatalysis Using Ruthenium Coordination Oligomers Adsorbed on Multiwalled Carbon Nanotubes. *Nat. Chem.* **2020**, *12* (11), 1060–1066. https://doi.org/10.1038/s41557-020-0548-7.

(34) Heinisch, T.; Pellizzoni, M.; Dürrenberger, M.; Tinberg, C. E.; Köhler, V.; Klehr, J.; Häussinger, D.; Baker, D.; Ward, T. R. Improving the Catalytic Performance of an Artificial Metalloenzyme by Computational Design. *J. Am. Chem. Soc.* **2015**, *137* (32), 10414–10419. https://doi.org/10.1021/jacs.5b06622.